UNIVERSITEIT VAN AMSTERDAM

UNIVERSITEIT VAN AMSTERDAM
&
VRIJE UNIVERSITEIT VAN AMSTERDAM

FACULTY OF SCIENCE

Evolutionary Modeling of Magnetic Binaries

Author:
Dani van Enk, 11823526
Report Bachelor Project
Physics and Astronomy
Size 15 EC
Conducted between
February 2, 2020
& August 20, 2020

Supervisor:
Alex de Koter
Examiner:
Lex Kaper
Institute:
Anton Pannekoek Institute

Submitted in partial fulfillment of the requirements for the BSc degree in Bachlor of Physics and Astronomy (jd) of the Universiteit van Amsterdam & Vrije Universiteit van Amsterdam

August 20, 2020

Abstract

In this work, the effect of surface magnetic fields on binary evolution has been studied. A valuable sample of binary systems has been acquired. This set contains close binary systems where at least one of the components has been observed to have a magnetic field. In such binary systems; the spin, orbital period of the stars and orbital evolution are affected by the magnetic field. Close binary systems provide constraints for the origin of the magnetic field. Currently, stellar mergers and initial environmental conditions have been proposed as the origin of the magnetic field. When a merger happens during the main-sequence phase of an initially triple system, the post-merger star rejuvenates which causes it to look younger. Since this can be seen in the evolution of the stars, this is tested using the Modules for Experiments in Stellar Astrophysics (MESA; version r12115) software instrument. MESA has been used to evaluate the physical characteristics of the HD 149277 system (focusing on spin and age). For the primary star, an age has been found between $20.7\,\mathrm{Myr}$ and $24.4\,\mathrm{Myr}$. The age of the secondary star has been found to be between $17.0\,\mathrm{Myr}$ and $24.8\,\mathrm{Myr}$. Both of the primary and secondary are past halfway of their main-sequence. Since both stars in the HD 149277 system have been found to have (within uncertainty) a similar age, a merger seems ruled out for the origin of the magnetic field. If a merger had happened, the signs of such rejuvenation would show and the stellar ages would lie further apart. However, the occurrence of a pre- or early-main-sequence merger can not be ruled out. It has been concluded that the origin of the magnetic field is either i) from a pre-main-sequence or early main-sequence stellar merger, or ii) from the environmental conditions of the star.

Samenvatting

Sterren die zwaarder zijn dan de zon zijn erg zeldzaam in vergelijking tot sterren die lichter zijn dan de zon. Deze sterren hebben vaak een partner, dit zijn zogenaamde dubbelsterren. Slechts een kleine fractie van zware sterren heeft een magnetisch veld. Als een zware magnetische ster in een zogeheten nauw dubbelstersysteem zit, is er naast getijdeninteracties ook een magnetische remming die het ronddraaien van de ster kan afremmen. Deze nauwe zware magnetische dubbelstersystemen zijn extreem zeldzaam. Tijdens dit project is gekeken naar het effect van het magnetische veld op de evolutie van het dubbelstersysteem HD 149277. Met behulp van de Modules for Experiments in Stellar Astrophysics (MESA; version r12115) software kan de rol van magneetvelden op de evolutie van het systeem worden onderzocht.
De leeftijd die gevonden is voor de primaire en de secundaire ster, is ongeveer hetzelfde. Hieruit volgt dat het samensmelten van twee sterren gedurende de hoofdreeksfase van een initieel drie-voudig stersysteem waarschijnlijk niet de oorsprong kan zijn van het magnetisch veld. Dit betekent echter niet dat het samensmelten niet volledig is uitgesloten. Het samensmelten van 2 van de drie sterren die initieel gevormd werden, zou nog steeds gebeurd kunnen zijn in de vroege hoofdreeks- of pre-hoofdreeksfase. Een andere mogelijkheid is dat het magnetisch veld is ontstaan vanwege omgevingstoestanden van de moleculaire wolk waaruit de sterren zijn ontstaan.

Acknowledgments

I would like to thank my supervisors, dr. Zsolt Keszthelyi and prof. dr. Alex de Koter, for their help during the project as well as the members of the API massive star group for their input on the conclusions of my project. I would also like to thank Alex Ferraro and Frederick Groth for their help with MESA. The dataset used in this work has been acquired from dr. Matt Shultz. For the computations, this work has made use of the Dutch national e-infrastructure with support of the SURF Cooperative. I would like to thank Tom Wind for the talks we had about the subjects discussed in this work.

Contents

1 Introduction

Stars are everywhere around us and can be seen on a clear night in the sky. They are large rotating plasma balls held in equilibrium by self-gravity and a gas-pressure gradient. The most common type of stars are low (mass of less than $2\,\mathrm{M}_\odot$) and intermediate (mass between $2\,\mathrm{M}_\odot$ and $8\,\mathrm{M}_\odot$) mass stars. More massive (mass more than $8\,\mathrm{M}_\odot$) stars are fairly rare. Stars create the elements in the universe through their nuclear fusion. Massive stars create a large fraction of heavy elements during their lives and at the end of their lives when they explode in a core-collapse supernova. Stars are thus the element factories of the universe. Massive stars are also the progenitors of gravitational waves, which are caused when neutron stars or black holes merge. To study stars in more detail, the evolution of these stars needs to be looked at (Lamers & Levesque 2017; Langer 2012; Maeder 2009). The properties of the star are derived from spectroscopy, photometry and spectro-polarimetric measurements. These are crucial to the study of individual and groups of stars.
Recent studies revealed that of massive OB stars, about 7% has a surface magnetic field which can be observed (Fossati et al. 2015; Grunhut et al. 2017). Those magnetic fields are mostly dipolar and stable. They are also quite strong and on the order of kG. These surface magnetic fields are extremely important for the evolution of massive stars. Binarity also has a significant impact on the evolution of stars. Massive stars do not have a convective surface like intermediate and low mass stars. This means that the origin of magnetic fields in massive stars is different from that of lower mass stars. For the origin of magnetic fields in massive stars, there are currently two running theories: environmental conditions and merging.

1.1 Environmental Conditions

One of these theories is described in Mestel (2003). According to this theory, the magnetic field is generated by environmental conditions. He describes multiple options for what the origin of the magnetic field could be. Firstly, the magnetic field may be a fossil field, i.e. leftover of the field of the molecular cloud, which decays slowly. This means that when the molecular cloud contracts to form a star, it attains part of this magnetic field. Next, the fossil field may be built by a dynamo in the pre-zero-age-main-sequence (pre-ZAMS) convective era of the star. This could be frozen in in the star. In Braithwaite & Spruit (2004) and Braithwaite & Nordlund (2006), numerical models have been constructed and from those models, it was concluded that the dynamo built magnetic field could relax into a stable equilibrium from a random unstable initial field.

1.2 Mergers

According to the other theory, the magnetic field would be formed because of a merger in the pre-main-sequence (pre-MS) or main-sequence (MS) phase. This theory is first described in Ferrario et al. (2009). The merger of two stars in an initially triple system would result in a binary where one of the stars is magnetic and the

other star is not. The star that is the result of the merger rejuvenates and becomes a blue straggler. This is a bright blue MS-star which is more luminous and bluer than other stars of the same age. The fields resulting from a merger would be relatively strong. This theory was expanded on by Schneider et al. (2016, 2019, 2020), by finding merger candidates and preforming 3D simulations on them. This was achieved by amplifying the magnetic fields from initial "seed" fields in the event of a merger.

1.3 Close Binaries

About all massive stars have been found to be in a binary system (Sana et al. 2012, 2014). Of massive stars, more than 70% will interact with a companion at the same point in their stellar evolution. When stars in a binary are close enough, the orbital angular momentum will affect the spin of the star. From this can be concluded that the rotational period and orbital period will change during the evolution of a binary system. Of the massive stars in a close binary, only about 2% has been found to have surface fossil magnetic fields (Alecian et al. 2015).

1.4 Structure of this work

This work will focus on this 2% binaries to study the effect of binarity and magnetism and tries to tie these effects on the origin of the surface fossil magnetic field.
The basic structure of this work is as follows. In section 2, some analysis will be done on a small sample set of magnetic binaries. Then in section 2.2, a closer look will be taken at one of the sample systems HD 149277. Next in section 3, some analysis will be done on the tidal interaction and magnetic braking timescales. In section 4, MESA will be used to generate evolutionary tracks of HD 149277 with the aim to find the initial parameters for this system when it has a magnetic field and when not. Lastly, in section 5, the findings of this work will be discussed.

2 Sample Stars

2.1 Sample exploration

At present, there is only a small number of close massive magnetic binary systems known. These systems are described in Shultz et al. (2018b); these are: HD 5550 (Alecian et al. 2016), HD 36485 (Leone et al. 2010), HD 37017 (Bolton et al. 1998), HD 62658 (Shultz et al. 2019), HD 66051 (Kochukhov et al. 2018), HD 98088 (Folsom et al. 2013), HD 136504 (Pablo et al. 2019), HD 149277 (González et al. 2018; Shultz 2016), HD 156324 (Shultz et al. 2018a), HD 161701 (González et al. 2014), BD-195044L (Landstreet et al. 2017). Their stellar and binary parameters are summarized in table 1, 2 and 3. To our knowledge, the data present is the most up to date compilation of the known close massive magnetic binaries available. The data is mainly based on Shultz et al. (2018b) but has been updated with values from the source papers of the systems. In the sample systems, Plaskett's star (an O+O

binary star system; Grunhut et al. 2013) has been excluded as it is a very special case and this work will focus more on the A and B spectral type stars.

The parameters shown in table 1, 2 and 3 have been derived from the spectra of the corresponding stars. Parameters such as radius, mass & gravitational acceleration have been derived from the width of the absorption lines in the spectrum, distance and absolute flux. Parameters such as spectral type and radial velocity have been derived from the relative strength and position of the absorption lines. Other parameters, such as the orbital period have been derived from the radial velocity curves. The magnetic field strength has been derived from spectro-polarimetric measurements, exploiting the Zeeman effect and advanced polarimetric techniques. Some of these parameters have not been determined with high certainty (like age, mass, gravitational acceleration, effective temperature), while other parameters have small uncertainties (like orbital period, rotational period, mass ratio). All of the systems in the sample are in our own galaxy and thus have a galactic metallicity.

Of the 11 binary systems in which surface fields have been detected, eight systems have a magnetic field in only the primary and two systems have a magnetic field in only the secondary. One system has magnetic fields detected in both components.

Table 1: Stellar parameters of the sample systems. It contains the name of the system, the component identifier, the radial velocity amplitude of the binary orbit K, the stellar the mass M, the dipolar magnetic field strength $B_{\rm d}$, the effective temperature $T_{\rm eff}$. The errorbars of HD161701 & BD-195044L have not been found for the dipolar magnetic field. For HD 36485, HD 37017, HD 149277, BD-195044L either the upper limit for the dipolar magnetic field has not been mentioned, or it has been mentioned to be not present.

System	Component	K (km/s)	M ($M_\odot$)	$B_{\rm d}$ (G)	$T_{\rm eff}$ (K)
HD 5550	A	24.97 ± 0.17	2.5 ± 0.01	65 ± 20	11400 ± 300
	B	38.58 ± 0.11	1.7 ± 0.01	0 ± 40	7800 ± 150
HD 36485	A	8.82 ± 0.4	6.3 ± 0.2	8800 ± 200	20000 ± 2000
	B	25.3 ± 0.6	2.4 ± 0.2	0	10000 ± 2000
HD 37017	A	30.8 ± 1.1	8.4 ± 0.1	8400 ± 900	21000 ± 2000
	B	90.4 ± 0.9	4.2 ± 0.1	0	14000 ± 1500
HD 62658	A	117 ± 0.1	3.2 ± 0.0007	0 ± 110	12300 ± 1000
	B	117 ± 0.2	3.16 ± 0.0007	750 ± 170	12300 ± 1000
HD 66051	A	76.6 ± 0.5	3.2 ± 0.02	600 ± 170	12100 ± 1000
	B	137.9 ± 0.5	1.8 ± 0.02	0 ± 170	8100 ± 800
HD 98088	A	73.31 ± 0.26	2.19 ± 0.01	3850 ± 450	8300 ± 300
	B	100.7 ± 0.43	1.67 ± 0.01	0 ± 1550	7500 ± 300
HD 136504	Aa	54.26 ± 0.08	7.6 ± 0.003	780 ± 80	20500 ± 500
	Ab	64.98 ± 0.08	6.4 ± 0.003	470 ± 200	18500 ± 500
HD 149277	**A**	$\mathbf{108.8 \pm 0.1}$	$\mathbf{8.75 \pm 0.4}$	$\mathbf{10200 \pm 1200}$	$\mathbf{20000 \pm 2000}$
	B	$\mathbf{119.9 \pm 0.1}$	$\mathbf{7.98 \pm 0.43}$	**0**	$\mathbf{19000 \pm 2000}$
HD 156324	Aa	51.4 ± 0.8	8.7 ± 0.07	13600 ± 3000	22000 ± 3000
	Ab	134.7 ± 1.3	3.4 ± 0.07	0 ± 2600	15000 ± 1500
HD 161701	A	60.24 ± 0.29	4 ± 0.01	0 ± 50	12400 ± 300
	B	101.31 ± 0.26	2.4 ± 0.01	750	9750 ± 300
BD-195044L	A	33.73 ± 0.36	3.4 ± 0.03	1400	13200 ± 600
	B	49.88 ± 0.38	2.3 ± 0.03	0	10000 ± 500

The orbital periods of the sample stars range between about $4.5\,\mathrm{d}$ and $30\,\mathrm{d}$, their

Table 2: Stellar parameters of the sample systems (continued). It contains the name of the system, the component identifier, the logarithm of the surface gravitational acceleration $log(g)$, the spectral type, the magnetic obliquity β and the projected rotational velocity $v\,sin(i)$.

System	Component	$log(g)$ (cm/s^2)	Spectral Type	β (deg)	$v\,sin(i)$ (km/s^{-1})
HD 5550	A	4 ± 3.5	Ap	156 ± 17	4 ± 2.1
	B	4 ± 4.5	Am	0	2.4 ± 1.1
HD 36485	A	4.2 ± 0.2	B3p	52	32
	B	4.3 ± 0.2	A	0	32
HD 37017	A	4.1 ± 0.2	B2V	2.6454 ± 0.0016	-
	B	4.25 ± 0.25	B1.5V	0	-
HD 62658	A	4.191 ± 0.002	B9	0	-
	B	4.212 ± 0.002	Ap	80.5 ± 15.5	-
HD 66051	A	4.05 ± 0.01	A0	-	-
	B	4.49 ± 0.02	Ap	-	-
HD 98088	A	3.9 ± 0.09	Ap	80 ± 5	-
	B	4.16 ± 0.12	Am	0	-
HD 136504	Aa	3.97 ± 0.15	B3	-	-
	Ab	4.13 ± 0.15	B3	-	-
HD 149277	**A**	$\mathbf{3.75 \pm 0.15}$	**B2IV/V**	**-**	**-**
	B	$\mathbf{3.85 \pm 0.15}$	**B3**	**-**	**-**
HD 156324	Aa	4 ± 0.3	B2V	71 ± 2	53 ± 10
	Ab	4.3 ± 0.3	B5V	0	32 ± 10
HD 161701	A	3.76 ± 0.03	B9	-	16.8 ± 0.6
	B	4.15 ± 0.13	Ap	-	7.6 ± 1.1
BD-195044L	A	4.25 ± 0.13	Bp	26 ± 9	13.8 ± 0.4
	B	4.26 ± 0.13	Ap	0	6.3 ± 0.2

eccentricity is anywhere from circular to a fairly elliptical orbit. The mass ratio[1] is anywhere from near 1 to 2.5. The obliquity is missing for the systems where it could not be found in the source papers.
The distribution of properties of the systems is visualized using some plots. In figure 1, it can be seen that most of the systems with near-circular orbits all have an orbital period lower than $15\,\mathrm{d}$ and the systems with a more elliptical orbit favor a longer orbital period.
In figure 2, the $log(g)$-T_{eff} values of all the components of the sample systems are plotted. A tentative correlation can be seen, where a higher gravitational acceleration corresponds to a lower effective temperature.

2.2 HD 149277

The system that is explored here is HD 149277 (González et al. 2018; Shultz et al. 2018b, 2019; Shultz 2016); it is marked in figure 1 and figure 2 and its stellar/system parameters can be seen in tables 1, 2 and 3 in bold. Compared to the other sample systems, both components have a relatively high effective temperature and high gravitational acceleration. Compared to the other sample systems, it has an

[1]In table 3, the mass ratio is mentioned to be M_1/M_2, this is $\frac{1}{q}$, it'll be mentioned as q from now on.

Table 3: Binary parameters of the sample systems. It contains the name of the system, the orbital period $P_{\rm orb}$, eccentricity e, the mass ratio M_1/M_2 and the inclination i.

System	P_{orb} (d)	e	M_1/M_2	i (deg)
HD5550	6.82	0.006 ± 0.001	1.47 ± 0.01	24 ± 30
HD36485	29.978498	0.29 ± 0.02	2.6 ± 0.2	12 ± 3
HD37017	18.6561	0.45 ± 0.008	2.02 ± 0.1	-
HD62658	4.752212	0.0042 ± 0.0004	1.012 ± 0.0007	83.6037 ± 0.009
HD66051	4.749	0	1.8 ± 0.02	86.148 ± 0.08
HD98088	5.905	0.184 ± 0.0025	1.31 ± 0.01	69 ± 2
HD136504	4.5597	0.28 ± 0.001	1.19 ± 0.003	-
HD149277	**11.5192(5)**	$\mathbf{0.236 \pm 0.004}$	$\mathbf{1.1 \pm 0.4}$	**-**
HD156324	1.5805279	0 ± 0.0028	2.57 ± 0.07	25.6 ± 2.2
HD161701	12.451	0.0043 ± 0.0023	1.67 ± 0.01	72 ± 2
BD-195044L	17.63	0.4738 ± 0.0063	1.47 ± 0.03	30.3 ± 0.6

average orbital period and eccentricity. This system is interesting to look at because it has a magnetic field strength of $10\,\mathrm{kG}$, which is high compared to the other sample systems. It is also interesting that the mass ratio is near 1. This means that the stars could be really similar if they are in a pre-interaction phase. Some of the systems in the sample have chemical peculiarities. These are denoted with the letter ”p” in the spectral type column of table 2. However, HD 149277 is not such a system. Therefore it is considered to be a non-peculiar B-type star system.

3 Timescales

3.1 Interactions

When the components of a binary system orbit each other close enough, the interactions between them (e.g., tidal interaction, mass transfer episodes & merging) can happen in their MS-phase. These interactions cause spin-orbit coupling to occur when close. The orbit is enlarged by the mass-loss of the star during its evolution. The spin of the star is affected by the tidal interactions between the two stars. If one of the components in the binary system has a magnetic field, this will also affect the spin evolution of the star. The winds of the star interact with the magnetic field and are confined in the magnetosphere of the star. It is eventually channeled back via the magnetic field lines onto the star through mass-loss quenching (Owocki et al. 2016). The mass lost from the star carries angular momentum with it.
Additionally, the magnetic fields provide a very effective way of transporting and removing angular momentum from the star. In a rotating star, the azimuthal bending of the magnetic field leads to angular momentum loss; this is more commonly known as magnetic braking. This combination of mass-loss quenching and magnetic braking affects the spin of the star. A non-magnetic star has a stronger mass-loss than a magnetic star (where mass-loss quenching is happening).

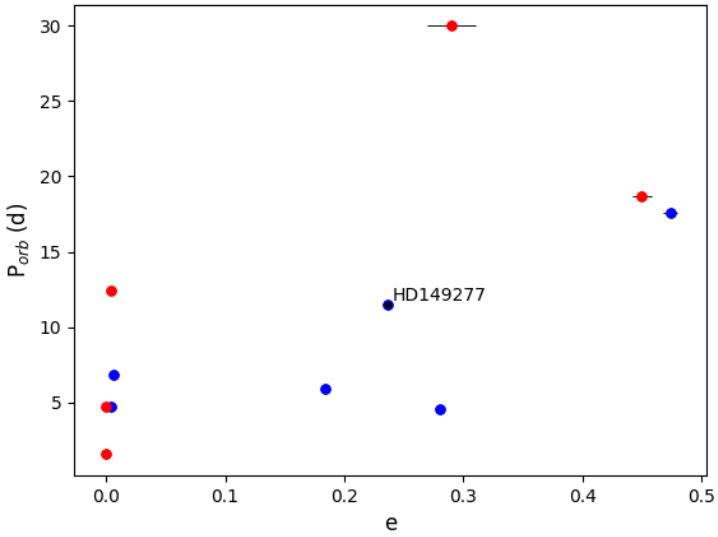

Figure 1: In this figure, the sample systems are shown by their eccentricity e and orbital period P_{orb}. The marker with a black dot is the HD 149277 system. This figure is color-coded in terms of mass ratio (M_1/M_2). Blue stands for $M_1/M_2 \leq 1.5$ and red stands for $M_1/M_2 > 1.5$

3.2 Timescales

Next, the timescales for the tidal interaction and magnetic braking were studied. The same analytical approach was used as in Song et al. (2018). In that work, the change in the total angular moment is to be divided into a component caused by tidal interaction and a component due to magnetic braking. A circular orbit was adopted. For the tidal interaction, the following formula has been described (assuming solid body rotation) by Zahn (1977),

$$\left(\frac{dJ}{dt}\right)_{\text{tides}} = -3MR^2(\Omega - \omega_{\text{orb}})\sqrt{\frac{GM}{R^3}}q^2\left(\frac{R}{a}\right)^6 E_2 s_{22}^{5/3}, \tag{1}$$

where J is the total angular momentum, M the mass of the primary, R the radius of the primary, Ω the spin angular velocity, ω_{orb} the orbital angular velocity, q is the mass ratio M_2/M_1, a the distance between both components in the system, E_2 is the tidal coefficient described by Yoon et al. (2010) as

$$E_2 = 10^{-1.37}\left(\frac{R}{R_{\text{conv}}}\right)^8, \tag{2}$$

where R_{conv} is the convective core radius,

$$s_{22} = 2(\Omega - \omega_{\text{orb}})\sqrt{\frac{R^3}{GM}}, \tag{3}$$

is the dimensionless tidal frequency as it is described in Zahn (1977). For the change in total angular momentum because of the magnetic braking Song et al. (2018)

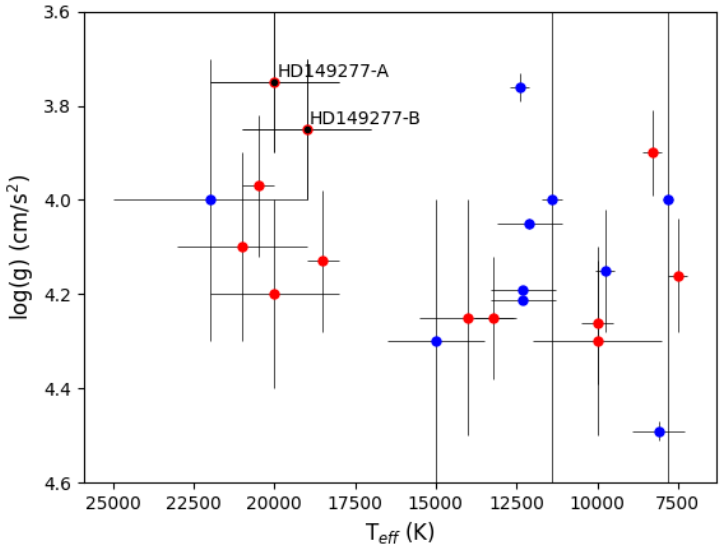

Figure 2: In this figure, the sample systems are shown by their effective temperature T_{eff} and logarithmic of the gravitational acceleration $log(g)$. The markers with a black dot are the components of the HD 149277 system. The limits are scaled such that the data is shown correctly; this causes some of the error bars to fall outside of the figure. This figure is color-coded with a threshold of an eccentricity of 0.1. Blue stands for $e \leq 0.1$ and red stands for $e > 0.1$

combine the confinement factor described in ud-Doula et al. (2008) and the formula for the total angular momentum of a thin spherical shell, which becomes

$$\left(\frac{dJ}{dt}\right)_{\text{tides}} = \frac{2}{3}\dot{M}\Omega R^2(.29 + \sqrt[4]{\eta_* + .25})^2, \tag{4}$$

where $\dot{M}$ is the mass-loss and η_* is the wind magnetic confinement parameter at the equator, given by

$$\eta_* = \frac{B_{\text{eq}}^2 R^2}{\dot{M} v_\infty}, \tag{5}$$

and is described in ud-Doula & Owocki (2002), B_{eq} is here the magnetic field at the equator and v_∞ is the wind terminal speed.
Combining equation 1 and 4, Song et al. (2018) defines a ratio between the timescale of both equations. It is defined as

$$\tau = \frac{\tau_{\text{tides}}}{\tau_{\text{mb}}} = \frac{\left(J/\frac{dJ}{dt}\right)_{\text{tides}}}{\left(J/\frac{dJ}{dt}\right)_{\text{mb}}} = \frac{\frac{2}{3}\dot{M}\Omega R^2(.29 + \sqrt[4]{\eta_* + .25})^2}{3MR^2|\Omega - \omega_{\text{orb}}|\sqrt{\frac{GM}{R^3}}q^2\left(\frac{R}{a}\right)^6 E_2 s_{22}^{5/3}}, \tag{6}$$

since the timescales are always positive, the absolute value of $\Omega - \omega_{\text{orb}}$ is used.
The wind terminal speed can be expressed as a factor times the escape velocity ($v_\infty = f_{\text{vinf}} \cdot v_{\text{esc}}$). This factor is: 0.7 for an effective temperature smaller than $12\,\text{kK}$; 1.3 for an effective temperature between 12 and $21\,\text{kK}$; 2.6 for an effective

temperature larger than $21\,\mathrm{kK}$ (Lamers et al. 1995). When using Kepler's law, the orbital separation can be found using the orbital period. In Song et al. (2018), $\omega_{\mathrm{orb}} = 2\pi/P_{\mathrm{orb}}$ and $\Omega = f2\pi/P_{\mathrm{orb}}$ is used to reduce the angular velocity to the orbital period. f is here the fraction between the spin and orbital angular velocity ($\Omega/\omega_{\mathrm{orb}}$).
If this ratio in equation 6 is equal to 1, the change in total angular momentum is the same for tidal interaction and magnetic braking. During the interaction phase of the system, the system will strive towards this equilibrium between tidal interaction and magnetic braking. When this equilibrium has been set in, the rotational velocity will be equal to the equilibrium velocity.

Table 4: In this table, the assumed standard values used to input in equation 6 are shown. The mass M, radius R & effective temperature T_{eff} are considered to be ZAMS parameters and thus will be changed simultaneously.

Parameter	Value
$\mathrm{M}_{primary}$ ($\mathrm{M}_\odot$)	10
R ($\mathrm{R}_\odot$)	5.6
T_{eff} (K)	22000
P_{orb} (d)	0 to 10
q	.7
f	0.01
$\dot{M}$ ($\mathrm{M}_\odot$/yr)	$1\cdot 10^{-9}$
B_{eq} (G)	10000
R_{conv}/R	20%

3.3 Analytical analysis

In Song et al. (2018), the timescale values have been studied while changing the fraction f and the equatorial magnetic field strength. This work also added a change of the ZAMS parameters (mass, effective temperature & radius), the mass ratio and the mass-loss rate. The same has been done, often making the same assumptions as in Song et al. (2018). The orbital period has been assumed between $0\,\mathrm{d}$ and $10\,\mathrm{d}$. The total angular momentum has been assumed equal to the spin angular momentum. In differentially rotating models, the total angular momentum is considered as the angular momentum of the stellar layers where the tides deposit or remove angular momentum. Thus the orbital angular momentum will only play a role when some resonance has been achieved (Song et al. 2013). In this work, some of the assumptions are different from Song et al. (2018); these include the mass-loss rate and the R/R_{conv} ratio. The assumed standard values can be seen in table 4.
In figures 3 through 5, the analytical results for the timescales for different orbital periods and parameters are displayed. If a parameter affects the timescale, multiple lines can be seen. The lines will go from black (lowest parameter value) to white (highest parameter value).

Firstly, the mass-loss rate $\dot{M}$ is varied. Its value is changed between $1 \cdot 10^{-10}\,\mathrm{M}_\odot/\mathrm{yr}$ and $1 \cdot 10^{-4}\,\mathrm{M}_\odot/\mathrm{yr}$. In figure 3, it can be seen that for high $\dot{M}$ values magnetic braking is more prominent, for low values the tidal interaction is more prominent.

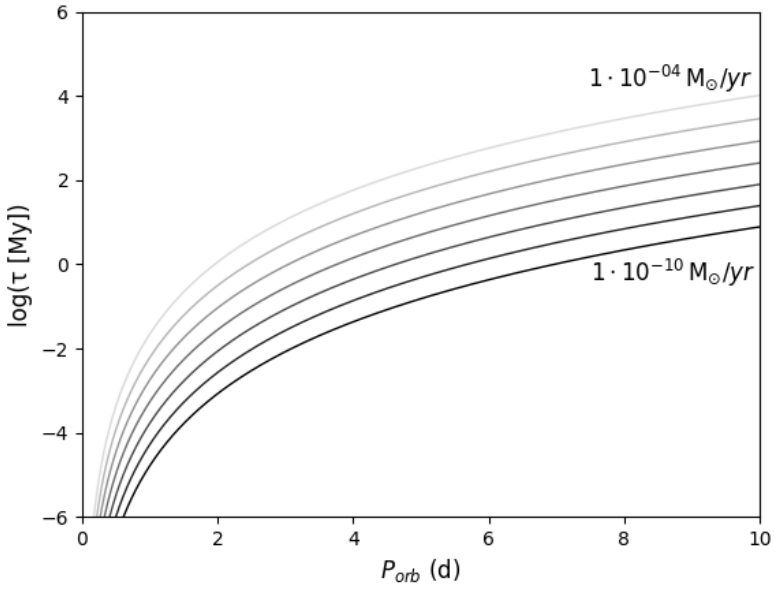

Figure 3: P_{orb} plotted against the timescale ratio in equation 6. Using this equation and the assumptions mentioned in section 3.3, the plots for different values of mass-loss $\dot{M}$ are shown. Starting from the bottom black plot with a $\dot{M}$ value of $1 \cdot 10^{-10}\,\mathrm{M}_\odot/\mathrm{yr}$ and ending at the white plot with a $\dot{M}$ value of $1 \cdot 10^{-4}\,\mathrm{M}_\odot/\mathrm{yr}$. For high $\dot{M}$ values the magnetic braking is more prominent, for low values tidal interaction is more prominent. In table 4, the assumed standard values can be seen.

Secondly, a change in ZAMS parameters is studied. A low-mass star (mass: $0.1\,\mathrm{M}_\odot$, effective temperature: $2.9\,\mathrm{kK}$, radius: $0.16\,\mathrm{R}_\odot$) and high-mass star (mass: $60\,\mathrm{M}_\odot$, effective temperature: $44.5\,\mathrm{kK}$, radius: $15\,\mathrm{R}_\odot$) have been compared. The masses of the steps for the ZAMS parameters are: $0.1\,\mathrm{M}_\odot$, $0.5\,\mathrm{M}_\odot$, $0.75\,\mathrm{M}_\odot$, $1.0\,\mathrm{M}_\odot$, $1.5\,\mathrm{M}_\odot$, $3\,\mathrm{M}_\odot$, $5\,\mathrm{M}_\odot$, $10\,\mathrm{M}_\odot$, $15\,\mathrm{M}_\odot$, $25\,\mathrm{M}_\odot$, $60\,\mathrm{M}_\odot$. As can be seen in figure 4, for a high-mass star magnetic braking is more prominent. For low-mass stars tidal interactions are more prominent.

Thirdly, a change in mass ratio q is looked at; its value is changed between .1 and 1. In figure 5, it can be seen that for q values close to 1 the magnetic braking is more prominent, for low q values tidal interactions are more prominent.

Both tidal interactions and magnetism heavily affect the spin evolution of a star. However, magnetic braking is the most dependent on the various parameters. As the system tries to achieve an equilibrium between tidal interactions and magnetic braking, the rotational and orbital speeds will change until the equilibrium speed is achieved. If this does not happen, the magnetic star will spin down and become a slowly rotating star.

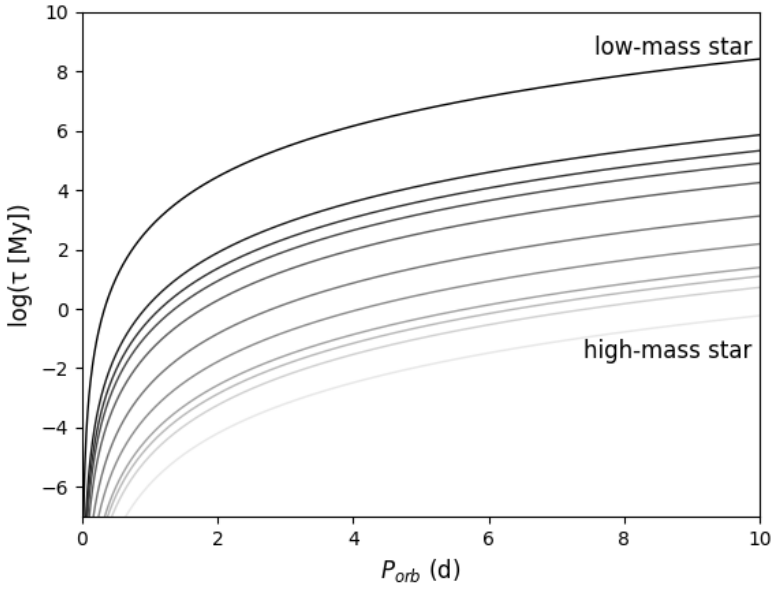

Figure 4: P_{orb} plotted against the timescale ratio in equation 6. Using this equation and the assumptions mentioned in section 3.3, the plots for different values of the ZAMS parameters are shown. Starting from the bottom black plot with a low-mass star with ZAMS parameters (mass: $0.1\,M_\odot$, effective temperature: $2900\,K$, radius: $0.16\,R_\odot$) and ending at the white plot with a high-mass star with ZAMS parameters (mass: $60\,M_\odot$, effective temperature: $44.5\,K$, radius: $15\,R_\odot$). The masses of the steps for the ZAMS parameters are: $0.1\,M_\odot$, $0.5\,M_\odot$, $0.75\,M_\odot$, $1.0\,M_\odot$, $1.5\,M_\odot$, $3\,M_\odot$, $5\,M_\odot$, $10\,M_\odot$, $15\,M_\odot$, $25\,M_\odot$, $60\,M_\odot$. For a high-mass star the tidal interaction is more prominent, for low-mass star the magnetic braking is more prominent. In table 4 the assumed standard values can be seen.

4 MESA

4.1 Introduction to MESA

Modules for Experiments in Stellar Astrophysics (MESA; version r12115) (Paxton et al. 2011, 2013, 2015, 2018, 2019) is an open-source 1D code used to simulate the evolution of a star. The MESA code has been expanded over the years. It currently can compute the evolution of the star from the pre-main-sequence phase to the more advanced past-main-sequence phases. Using this software, accurate simulations can be made of the full life-cycle of the star. The objects can have masses ranging from Gas Giant/Brown Dwarf masses to Supermassive stars. It simultaneously solves the structure and composition equations along with the nuclear reaction rates, opacity tables, etc. (see Paxton et al. (2011, 2013, 2015, 2018, 2019) for more about this). Each module is constructed as a separate Fortran library. Its star module contains up-to-date physical prescriptions to model the structure and evolution of stars. With its binary module, a binary system can be calculated with differentially rotating stars. These are undergoing mass transfer/loss and angular momentum transfer/loss.

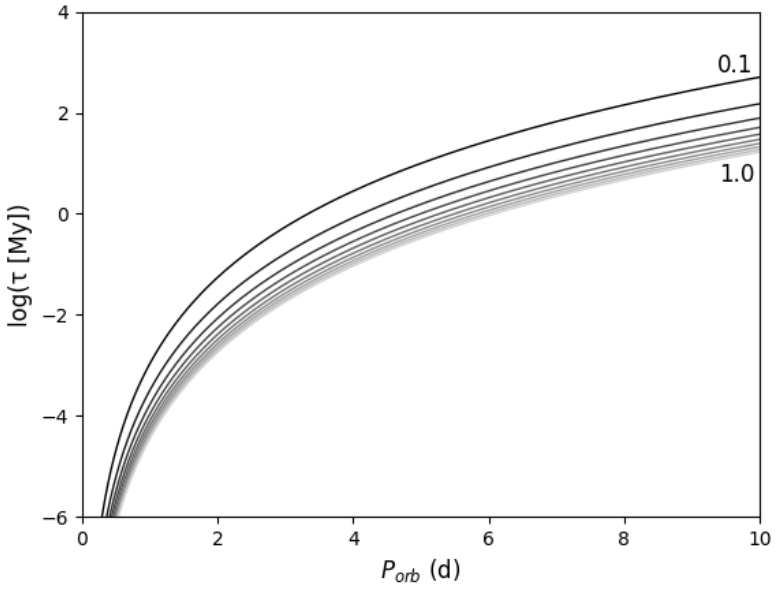

Figure 5: P_{orb} plotted against the timescale ratio in equation 6. Using this equation and the assumptions mentioned in section 3.3, the plots for different values of the mass ratio q are shown. Starting from the bottom black plot with a q value of .1 and ending at the white plot with a q value of 1. For small values of q the tidal interaction is more prominent, for large q the magnetic braking is more prominent. In table 4, the assumed standard values can be seen.

4.2 Method

The summer school lectures of J. Schwab (2013), S. de Mink (2017) & P. Marchant (2017) have been used to learn about input parameters and the run_star_extras module. In this work, two models have been computed; the first one where the surface magnetic field is absent (henceforth B0) and the second one where the surface magnetic field is present (henceforth B1). The input parameters can be divided into two categories. The first category includes the parameters that change depending on the fitting conditions, in this work the fitting conditions are the HD 149277 observation data seen as bold in tables 1, 2 & 3. The evolutionary tracks for the system will be fitted to these values. These first category parameters can be seen in the tables A5 & A6 and include the initial rotational speed of the star, the initial magnetic field strength, initial eccentricity, initial orbital period & initial masses of both the primary and secondary. In the second category fall all other parameters. The torque method and the magnetic evolution type need to be specified for the primary. Mass-loss quenching has been assumed and the parameters for magnetic braking, angular momentum & chemical mixing need to be set. In this work, it has been chosen to evolve both stars and tidal circularisation & tidal torque have been assumed as for a radiative envelope as described in Hurley et al. (2002). The stopping condition has been chosen to be when the Hydrogen-1 isotope mass fraction drops below $1 \cdot 10^{-5}$, in other words, when the star reaches the terminal-age-main-sequence.

MESA can be expanded using the run_extras module. Using in this module, the source code of MESA can be changed and thus the physics of MESA can be redefined. For the computations done here, the magnetic braking routine described in Keszthelyi et al. (2020) has been used. This routine expands onto the other_torque routine by assuming that the magnetic field strength is obtained from the equation for magnetic flux conservation,

$$B_{\rm p}(t)R^2(t) \;=\; B_{\rm p,0}R_0^2, \tag{7}$$

where surface magnetic polar field strength $B_{\rm p}$ scaled with the radius R is equal to the initial $B_{\rm p}$ strength scaled with the initial radius (Keszthelyi et al. 2019). Stars with a large surface magnetic field strength have been found to have a less effective mass-loss (ud-Doula & Owocki 2002; Bard & Townsend 2016) compared to non-magnetic stars, because of the mass-loss quenching. This may be expressed using the escaping wind fraction f_B which is equal to,

$$f_{\rm B} \;=\; \frac{\dot{M}}{\dot{M}_{\rm B=0}}, \tag{8}$$

where $\dot{M}$ is the mass-loss rate of the star and $\dot{M}_{\rm B=0}$ the mass-loss rate of the star if it had no magnetic field. Formula 4 have been used in Keszthelyi et al. (2019, 2020) to rewrite the magnetic and angular momentum routines in the MESA source code.
For the computations for HD 149277, the following assumptions have been made with regard to the Keszthelyi et al. routine. Firstly, the evolution of the magnetic field was assumed to follow magnetic flux conservation as described in formula 7. Secondly, the mass-loss quenching is described as in the other_wind part of the Keszthelyi et al. routine.

4.3 Tests

Before the results were gathered, a number of tests were performed to fit the evolutionary tracks to the observational data. In figure 6, the evolution of the rotational velocity of the primary star is shown. The magnetic field has been assumed to be $10\,\mathrm{kG}$ and the initial rotational velocities range between $300\,\mathrm{km/s}$ and $1 \cdot 10^{-5}\,\mathrm{km/s}$. For velocities higher than $1\,\mathrm{km/s}$ the star spins down. This happens because for rotational velocities (which are high) the magnetic braking is really effective in either i) spinning down the star or ii) slowing the rotation of the star (see formula 6). For velocities lower than $1\,\mathrm{km/s}$ the star spins up. For rotational velocities of $1 \cdot 10^{-1}\,\mathrm{km/s}$ and $1 \cdot 10^{-2}\,\mathrm{km/s}$, the star starts to spin down near the end of the main-sequence. Looking at formula 6, it can be concluded that the magnetic braking is less effective at lower rotational speeds. After about $10\,\mathrm{Myr}$ it can be seen that the rotational speed is able to overshoot the equilibrium speed. Once this happens magnetic braking and tidal interactions will try to correct this speed towards the equilibrium speed. The marker shown in the figure is the observed value and uncertainty of HD 149277.

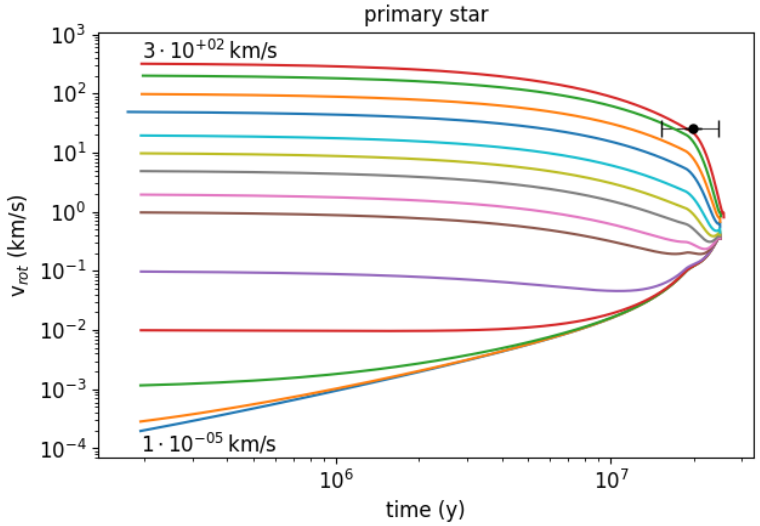

Figure 6: The rotational velocity evolution of multiple initial rotational velocities. The magnetic field strength has been assumed to be $10\,\mathrm{kG}$ and the initial rotational velocities range between $300\,\mathrm{km/s}$ and $1 \cdot 10^{-5}\,\mathrm{km/s}$. For velocities higher than $1\,\mathrm{km/s}$ the star spins down, for velocities smaller than $1\,\mathrm{km/s}$ the star spins up. After about $10\,\mathrm{Myr}$, the equilibrium rotational speed starts to set in. The marker shown in the figure is the observed value and uncertainty of HD 149277.

4.4 Results

The evolution of HD 149277 can be seen in figures 7, 8, 9 where the time is indicated via a color bar. The time evolution of the rotation period, orbital and separation of HD 149277 is given in figures 10 and 11. The evolution of HD 149277 has been computed for two models. These are the B0 model where the magnetic field is absent and the B1 model where the magnetic field is present. The parameters which are different between the B0 & B1 models are given in the tables A5 & A6. The markers shown in the figures are the observed values and uncertainties of HD 149277. The rotational period of the primary is very well known. The rotational period is not known for the secondary and thus the marker for it in figures 9-left and 10-left are not shown.

4.4.1 $log(g)$-T_{eff} Evolution

In figure 7, the $log(g)$-T_{eff} plane for the primary star (left) and the secondary star (right) can be seen. For the primary star (figure 7-left), the difference between the B0 & B1 models can be related to the mass-loss quenching of the primary. The primary star in the B1 model has an initial mass lower than the B0 model primary star; this is because of the fitting conditions. Because of this the $log(g)$-T_{eff} plane is slightly different for the B0 & B1 models. In the last stages of the main-sequence, the mass of in the B0 & B1 models diverge, the B0 model losing more mass and the B1 model only losing a small amount of mass. For the fitting of the evolutionary tracks

to the observational data of the HD 149277 system, the fitting to the $log(g)$-T_{eff} plane has been prioritized over the $log(L)$-T_{eff} plane.

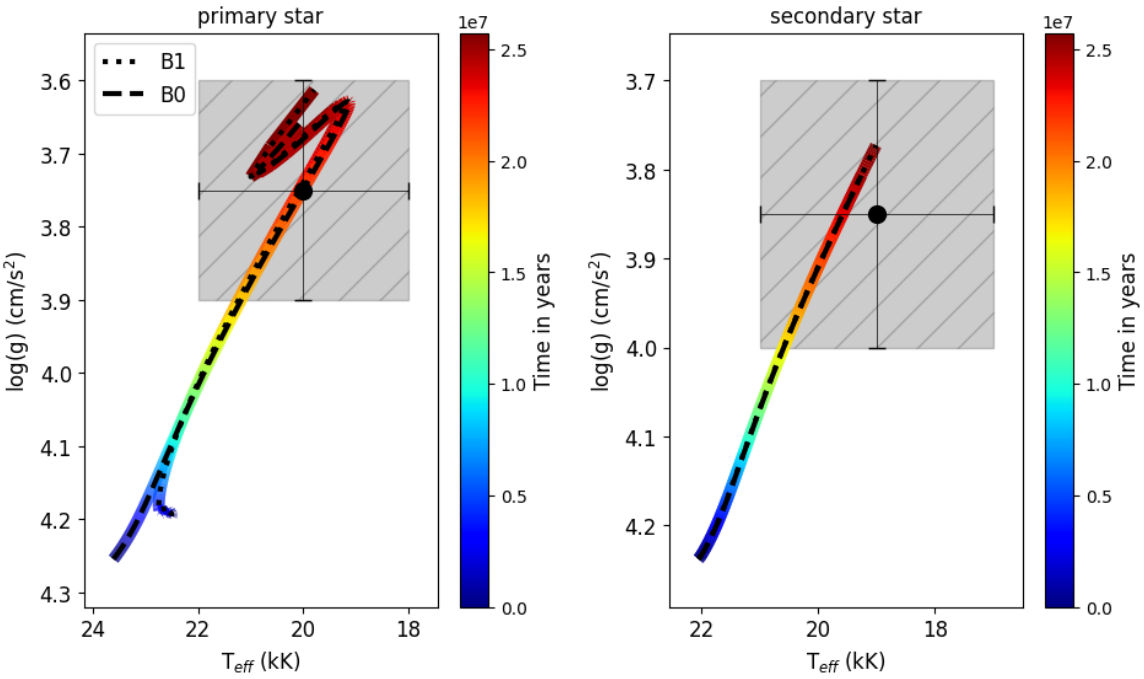

Figure 7: The $log(g)$-T_{eff} plane for the primary star (left) and the secondary star (right). The evolutionary tracks for both the non-magnetic (B0) & magnetic (B1) models are shown. In the left figure, a small difference can be seen between model B0 & B1. The evolutionary tracks of the secondary are identical. The markers shown in the figures are the observed values and uncertainties of HD 149277. The models have been fitted to these observed values for HD 149277. The primary star has in the B0 model an age between $17.0\,\text{Myr}$ and $25.7\,\text{Myr}$, in the B1 model it has an age between $18.8\,\text{Myr}$ and $25.7\,\text{Myr}$. The secondary star has in the B0 model an age between $17.0\,\text{Myr}$ and $24.8\,\text{Myr}$, in the B1 model an age between $17.8\,\text{Myr}$ and $24.8\,\text{Myr}$.

4.4.2 Orbital Period Evolution

In figure 8, the P_{orb}-e plane of the system can be seen. In figure 9, the P_{rot}-P_{orb} plane for the primary star (left) and the secondary star (right) are shown. For the B0 model, the increase in orbital period is because of the mass-loss of both the primary and secondary. For the B1 model, the increase in orbital period for the primary (figure 9-left) is amplified by magnetic braking of the primary. In the B1 model for the secondary (figure 9-right), the orbital period is increased by the mass-loss of the star. This is why the orbital period initial parameters are different for the B0 & B1 models.

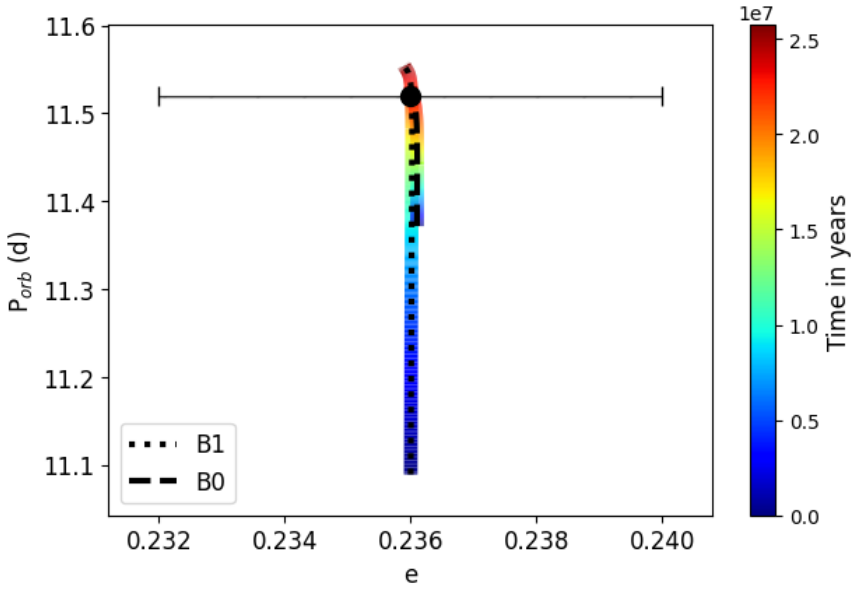

Figure 8: The evolution of the P_{orb}-e plane of the system. The evolutionary tracks for both the non-magnetic (B0) & magnetic (B1) models are shown. The marker shown in the figure is the observed values and uncertainties of HD 149277. The models have been fitted to these observed values for HD 149277. The magnetic field in the model B1 causes the orbital period to change more in the lifetime of the star than the orbital period of the B0 model. The primary star in the B0 model has an age between $23.7\,\mathrm{Myr}$ and $23.8\,\mathrm{Myr}$, in the B1 model it has an age between $21.6\,\mathrm{Myr}$ and $25.7\,\mathrm{Myr}$.

4.4.3 Rotational Period Evolution

In figure 9, the P_{rot}-P_{orb} plane and in figure 10, the P_{rot}-time plane for the primary star (left) and the secondary star (right) can be seen. The B0 model has an increase in the rotational period because of the mass-loss of the star. The total loss of angular momentum from the system increases the orbital period. This loss in angular momentum is due to the combined mass-loss of both components of the system. For the B1 model, the star spins down because of both the mass-loss and magnetic braking of the star. Since the magnetic field is far more efficient in spinning down the star, the effect can be seen more clearly in the B1 model. For the secondary, the rotational period change is the same for the B0 & B1 models; which can be seen in figure 10. The difference in orbital period seen in figure 9 has been explained in the previous subsection (Section 4.4.2).

It can be concluded for the B0 model, that the primary slows down from sub-$10\,\mathrm{d}$ rotation period to a rotation period of about $20\,\mathrm{d}$. For the B1 model, the primary starts with a rotational period of sub-$1\,\mathrm{d}$ and will end its MS evolution with a rotational period of over $100\,\mathrm{d}$. This means that the magnetic braking heavily influences the rotational period of the primary. From figure 10, it can be concluded that in the B0 model for the primary and the B0 & B1 model for the secondary, the star starts with spinning down slowly. As the mass-loss increases (see figure B13) the star slows down. When looking at the B1 model of the primary (figure 10-left), the star starts

spinning down slowly. Closer to the terminal-age-main-sequence, the star starts to expand and this causes the rotational period to increase drastically. Magnetic braking is only effective initially, as the field weakens the magnetic braking becomes less and less effective.

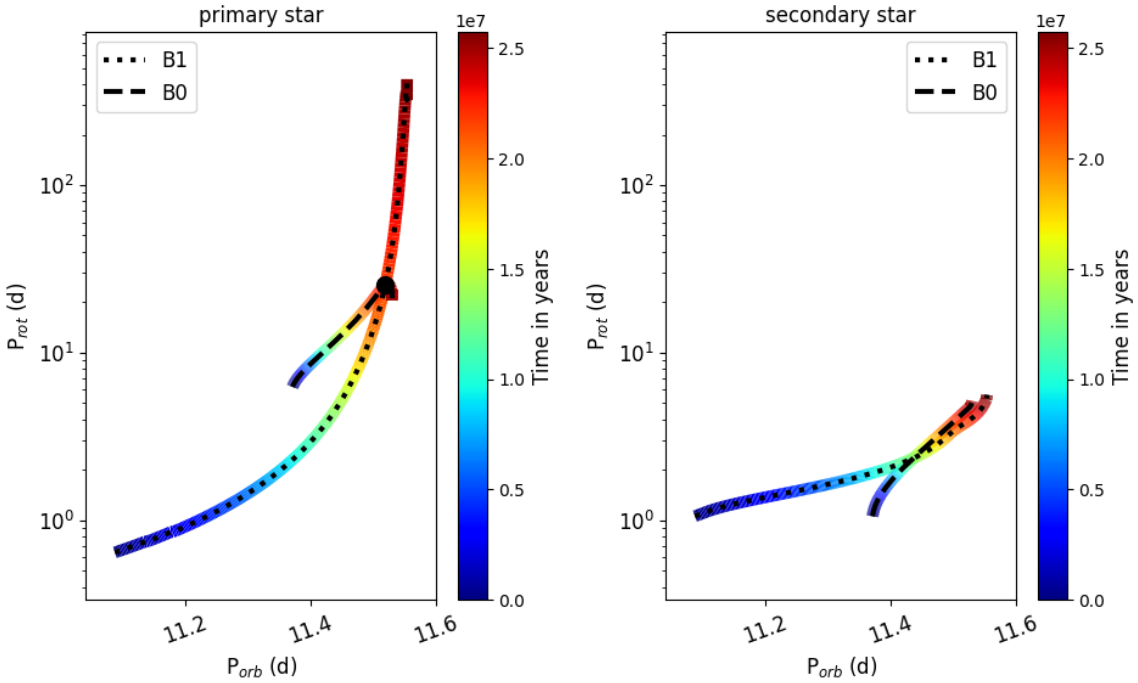

Figure 9: The P_{rot}-P_{orb} plane for the primary star (left) and the secondary star (right). For the primary, the evolutionary tracks for both the non-magnetic (B0) & magnetic (B1) models are shown. The marker shown in the figure is the observed values and uncertainties of HD 149277. The models have been fitted to these observed values for HD 149277. The magnetic field in B1 causes the orbital period to change more during the lifetime of the star then for model B0. For the orbital period, this effect can be seen for both the primary and secondary. When looking at the rotational period, the B0 model has a smaller increase in the rotational period than the B1 model. The primary star has in the B0 model an age between $23.8\,\mathrm{Myr}$ and $24.5\,\mathrm{Myr}$, in the B1 model it has an age between $21.6\,\mathrm{Myr}$ and $21.7\,\mathrm{Myr}$.

4.4.4 Binary Separation Evolution

In figure 11 the temporal evolution of the orbital separation can be seen. The same way the magnetic braking changes the rotational period more drastically, the orbital separation is changed more drastically in the B1 model. In the B0 model, the orbital separation is increased by the mass-loss of both stars in the system.

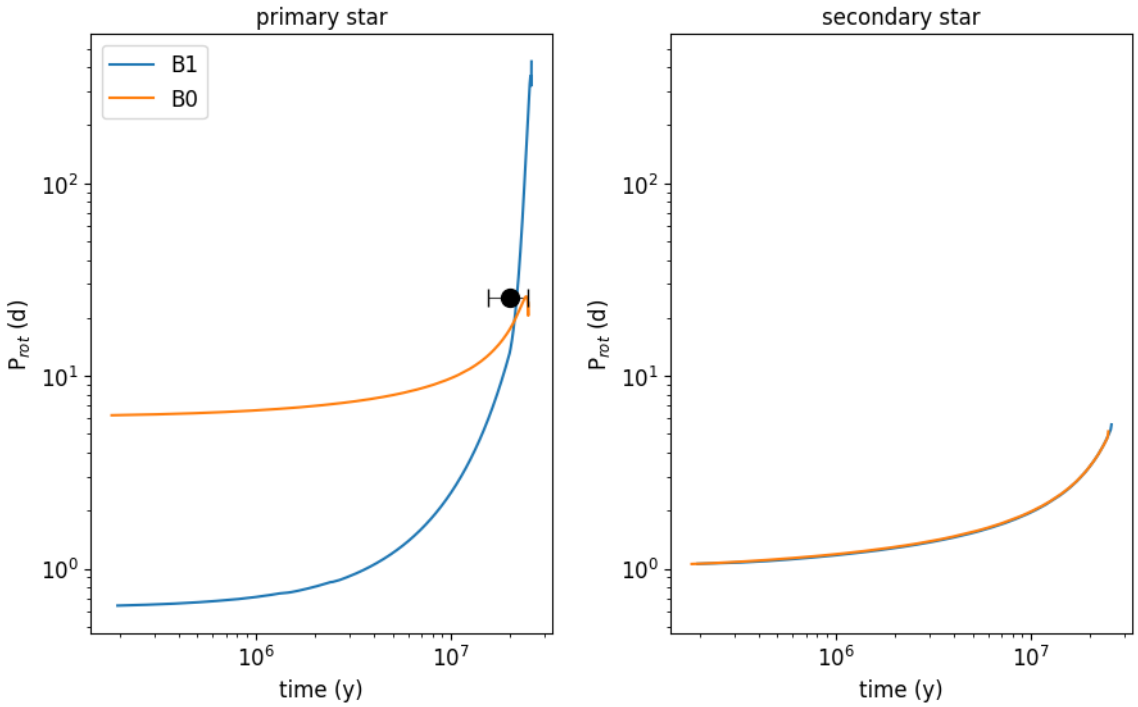

Figure 10: The $P_{\rm rot}$-time plane for the primary star (left) and the secondary star (right). The marker shown in the figure is the observed values and uncertainties of HD 149277. The models have been fitted to these observed values for HD 149277. For the primary, the evolutionary tracks for both the non-magnetic (B0) & magnetic (B1) models are shown. The B0 model has a smaller increase in the rotational period than the B1 model for the primary.

5 Conclusion

Following the work of Song et al. (2018), the timescale of tidal interactions and magnetic braking has been further studied. Its has been found that the ZAMS-parameters are the most effective in changing the timescales for both the magnetic braking and the tidal interaction, followed by the mass-loss and the mass ratio. During the evolution of the system, this causes a competition between magnetic effects and the effects of binarity. On the one hand, as the star loses mass; the effects of binarity will begin to become more prominent. On the other hand, the magnetic braking will remove angular momentum of the star and thus changing the rotational and orbital periods for the system. It has been found that in the HD 149277 system, the orbital separation is large enough that the magnetic field wins the battle to the effects of binarity. This can be seen in the orbit of the system and the rotation of the primary. The best fitted evolutionary tracks for the system have been found using the MESA software and the initial parameters in tables A5 & A6. For the B0 model, the age of the primary has been found to be between $21.6\,\mathrm{Myr}$ and $24.7\,\mathrm{Myr}$. For the B1 model, the age of the primary has been found to be between $20.7\,\mathrm{Myr}$ and $24.4\,\mathrm{Myr}$. The age of the secondary has been found to be between $17.0\,\mathrm{Myr}$ and $24.8\,\mathrm{Myr}$. The main-sequence duration of the system has been found to be $25.7\,\mathrm{Myr}$ for the pri-

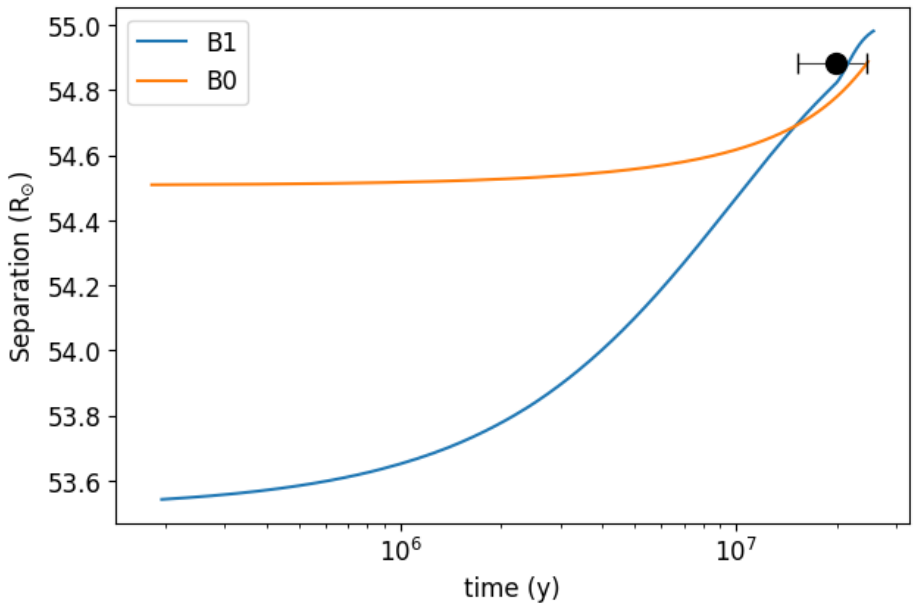

Figure 11: The temporal evolution of Separation-time plane for the system. For the primary, the evolutionary tracks for both the non-magnetic (B0) & magnetic (B1) models are shown. In the B0 model, the orbit is enlarged less than in the B1 model. The markers shown in the figures are the observed values and uncertainties of HD 149277.

mary and $24.8\,\mathrm{Myr}$ for the secondary.[2] This means that both stars are in their second half of their main-sequence phase, though the uncertainties on the constraints of the models are large. The age constraint seems to rule out the possibility that the magnetic field originated from a recent merger. If a merger had happened, the primary would have been rejuvenated and one would expect a significant difference in age between the primary and secondary. There is still a possibility that the merger could have happened in the pre-main-sequence or early main-sequence. If it happened this early on in the stellar evolution, the primary and secondary likely would still look similar. Alternatively, the magnetic field origin of the primary star of HD 149277 may lie in environmental conditions of the star-forming cloud or during the proto-stellar evolution. If this is indeed the case, a model needs to be created to explain why only one of the components of the system became magnetic. Continuing from this work, future work should try to look into modeling the pre-main-sequence phase of the system. This includes finding models that describe the merger theory and the environmental theory for the origin of the surface magnetic field. Also, more fitting constraints and lowering the uncertainties of the fitting constraints could be studied. Better fitting of the models should also be studied; this means fitting the parameters in a multidimensional grid style.

[2]These values and the values in 5 & 6 are model dependent, if a different stellar evolution code would be used. Different results can be found.

References

Alecian, E., Neiner, C., Wade, G. A., et al. 2015, in IAU Symposium, Vol. 307, New Windows on Massive Stars, ed. G. Meynet, C. Georgy, J. Groh, & P. Stee, 330–335 pages 2

Alecian, E., Tkachenko, A., Neiner, C., Folsom, C. P., & Leroy, B. 2016, A&A, 589, A47 pages 2

Bard, C. & Townsend, R. H. D. 2016, MNRAS, 462, 3672 pages 12

Bolton, C. T., Harmanec, P., Lyons, R. W., Odell, A. P., & Pyper, D. M. 1998, A&A, 337, 183 pages 2

Braithwaite, J. & Nordlund, Å. 2006, A&A, 450, 1077 pages 1

Braithwaite, J. & Spruit, H. C. 2004, Nature, 431, 819 pages 1

Ferrario, L., Pringle, J. E., Tout, C. A., & Wickramasinghe, D. T. 2009, MNRAS, 400, L71 pages 1

Folsom, C. P., Likuski, K., Wade, G. A., et al. 2013, MNRAS, 431, 1513 pages 2

Fossati, L., Castro, N., Schöller, M., et al. 2015, A&A, 582, A45 pages 1

González, J. F., Hubrig, S., Järvinen, S. P., & Schöller, M. 2018, MNRAS, 481, L30 pages 2, 4

González, J. F., Saffe, C., Castelli, F., et al. 2014, A&A, 561, A63 pages 2

Grunhut, J. H., Wade, G. A., Leutenegger, M., et al. 2013, MNRAS, 428, 1686 pages 3

Grunhut, J. H., Wade, G. A., Neiner, C., et al. 2017, MNRAS, 465, 2432 pages 1

Hurley, J. R., Tout, C. A., & Pols, O. R. 2002, MNRAS, 329, 897 pages 11

Keszthelyi, Z., Meynet, G., Georgy, C., et al. 2019, MNRAS, 485, 5843 pages 12

Keszthelyi, Z., Meynet, G., Shultz, M. E., et al. 2020, MNRAS, 493, 518 pages 12

Kochukhov, O., Johnston, C., Alecian, E., Wade, G. A., & BinaMIcS Collaboration. 2018, MNRAS, 478, 1749 pages 2

Lamers, H. J. G. L. M. & Levesque, E. M. 2017, Understanding Stellar Evolution pages 1

Lamers, H. J. G. L. M., Snow, T. P., & Lindholm, D. M. 1995, ApJ, 455, 269 pages 8

Landstreet, J. D., Kochukhov, O., Alecian, E., et al. 2017, A&A, 601, A129 pages 2

Langer, N. 2012, ARA&A, 50, 107 pages 1

Leone, F., Bohlender, D. A., Bolton, C. T., et al. 2010, MNRAS, 401, 2739 pages 2

Maeder, A. 2009, Physics, Formation and Evolution of Rotating Stars pages 1

Mestel, L. 2003, in Astronomical Society of the Pacific Conference Series, Vol. 305, Magnetic Fields in O, B and A Stars: Origin and Connection to Pulsation, Rotation and Mass Loss, ed. L. A. Balona, H. F. Henrichs, & R. Medupe, 3 pages 1

Owocki, S. P., ud-Doula, A., Sundqvist, J. O., et al. 2016, MNRAS, 462, 3830 pages 5

Pablo, H., Shultz, M., Fuller, J., et al. 2019, MNRAS, 488, 64 pages 2

Paxton, B., Bildsten, L., Dotter, A., et al. 2011, ApJS, 192, 3 pages 10

Paxton, B., Cantiello, M., Arras, P., et al. 2013, ApJS, 208, 4 pages 10

Paxton, B., Marchant, P., Schwab, J., et al. 2015, ApJS, 220, 15 pages 10

Paxton, B., Schwab, J., Bauer, E. B., et al. 2018, ApJS, 234, 34 pages 10

Paxton, B., Smolec, R., Schwab, J., et al. 2019, ApJS, 243, 10 pages 10

Sana, H., de Mink, S. E., de Koter, A., et al. 2012, Science, 337, 444 pages 2

Sana, H., Le Bouquin, J. B., Lacour, S., et al. 2014, ApJS, 215, 15 pages 2

Schneider, F. R. N., Ohlmann, S. T., Podsiadlowski, P., et al. 2020, MNRAS, 495, 2796 pages 2

Schneider, F. R. N., Ohlmann, S. T., Podsiadlowski, P., et al. 2019, Nature, 574, 211 pages 2

Schneider, F. R. N., Podsiadlowski, P., Langer, N., Castro, N., & Fossati, L. 2016, MNRAS, 457, 2355 pages 2

Shultz, M. 2016, PhD thesis, Queen's University (Canada) pages 2, 4

Shultz, M., Rivinius, T., Wade, G. A., et al. 2018a, MNRAS, 475, 839 pages 2

Shultz, M. E., Johnston, C., Labadie-Bartz, J., et al. 2019, MNRAS, 490, 4154 pages 2, 4, 21

Shultz, M. E., Wade, G. A., Rivinius, T., et al. 2018b, MNRAS, 475, 5144 pages 2, 4

Song, H. F., Maeder, A., Meynet, G., et al. 2013, A&A, 556, A100 pages 8

Song, H. F., Meynet, G., Maeder, A., et al. 2018, A&A, 609, A3 pages 6, 7, 8, 17

ud-Doula, A. & Owocki, S. P. 2002, ApJ, 576, 413 pages 7, 12

ud-Doula, A., Owocki, S. P., & Townsend, R. H. D. 2008, MNRAS, 385, 97 pages 7

Yoon, S. C., Woosley, S. E., & Langer, N. 2010, ApJ, 725, 940 pages 6

Zahn, J. P. 1977, A&A, 500, 121 pages 6

A Initial values

Table 5: In this table, the initial values used for the evolutionary (B0) model without a magnetic field has been specified.

	Magnetic Field off (B0)	
	Primary	Secondary
$v_{\rm rot}$ (km/s)	30 ± 20	200 ± 20
$B_{\rm p}$ (G)	0	0
M ($M_\odot$)	8.81 ± 0.41	8.01 ± 0.44
	System	
$P_{\rm orb}$ (d)	11.3708 ± 0.004	
e	0.2361 ± 0.004	

Table 6: In this table, the initial values used for the evolutionary (B1) model magnetic field has been specified.

	Magnetic Field on (B1)	
	Primary	Secondary
$v_{\rm rot}$ (km/s)	300 ± 20	200 ± 20
$B_{\rm p}$ (kG)	10 ± 4	0
M ($M_\odot$)	8.7501 ± 0.41	8.012 ± 0.44
	System	
$P_{\rm orb}$ (d)	11.08045 ± 0.004	
e	0.2360 ± 0.004	

B Extra figures

In this appendix section, extra figures are shown for the evolutionary tracks of the non-magnetic (B0, dashed) & magnetic (B1, dotted) models for the HD 149277 system (see tables A5 & A6. The age for HD 149277 has been adopted from Shultz et al. (2019).

In figure 12 & figure 13, the evolutionary tracks for the primary (left) and the secondary (right) are shown in the Hertzsprung-Russell (HR) diagram and the mass vs time diagram respectively. In the B1 model, the primary starts with a lower mass, hence lower luminosity than the primary in the B0 model. As the B0 model loses mass, it becomes similar to the B1 model. Near the end of the main-sequence, the B0 model has less mass than the B1 model. The B1 model loses less mass due to the mass-loss quenching.

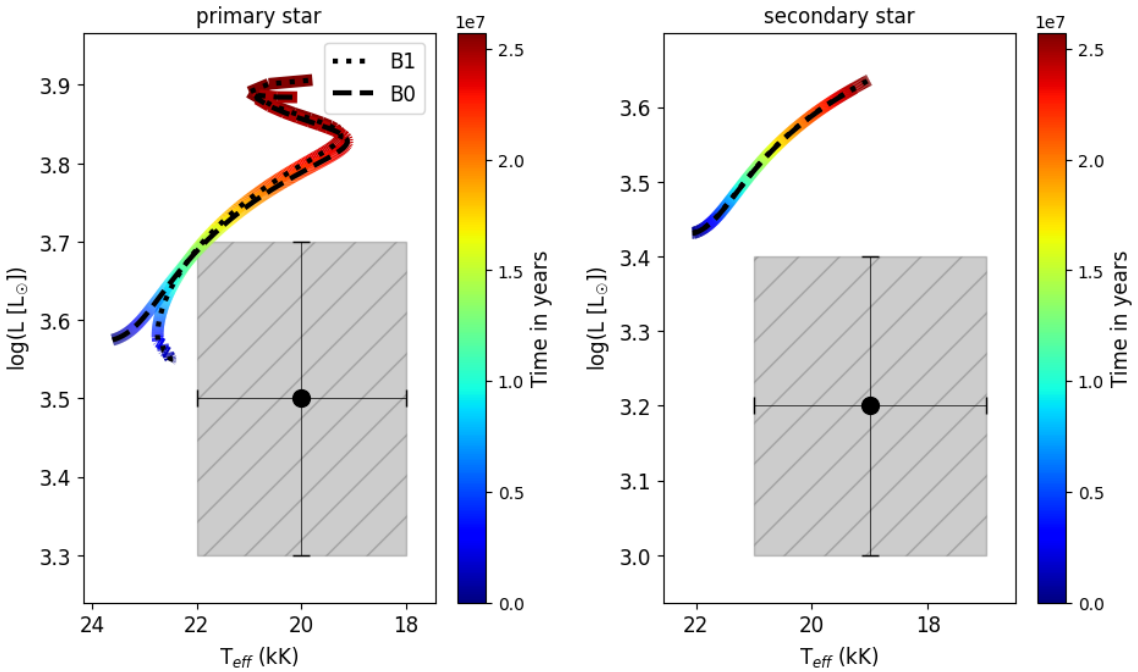

Figure 12: The Hertzsprung-Russell diagram for the primary star (left) and secondary star (right). The markers shown in the figures are the observed values and uncertainties of HD 149277. The models have been fitted to these observed values for HD 149277. In both panels, the evolutionary tracks for both the non-magnetic (B0) & magnetic (B1) models are shown. The color in these tracks indicates age. A small change between the B0 and B1 models of the primary is seen at the initial evolution phase.

In figure 14, the stellar and Roche radii of the B1 model for both the primary star (left panel) and the secondary star (right panel) can be seen. Since the stellar radius does not exceed the Roche radius of both components, Roche lobe overflow does not happen in the main-sequence phase of the system. This also means that mass transfer does not happen between the two stellar components in this part of their evolution.

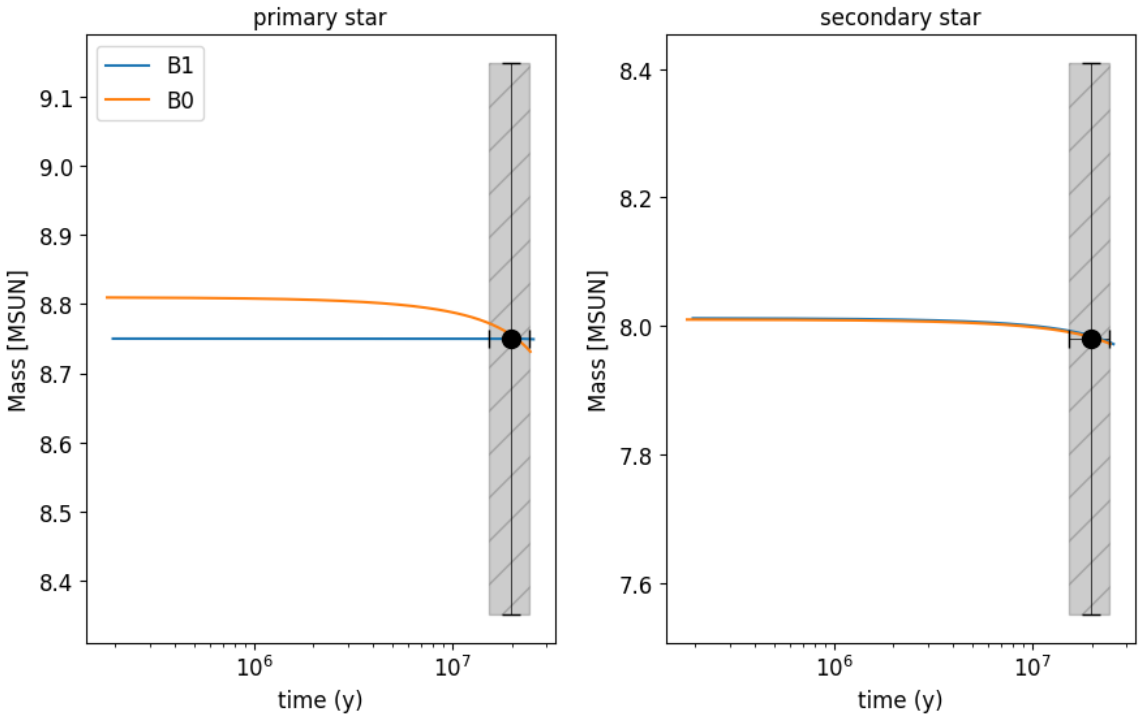

Figure 13: The mass-time plane for the primary star (left) and the secondary star (right). The markers shown in the figures are the observed values and uncertainties of HD 149277. The models have been fitted to these observed values for HD 149277. The evolutionary tracks for both the non-magnetic (B0) & magnetic (B1) models are shown up to the end of the main sequence. For the B1 model, the mass-loss of the star is really small in comparison to the B0 mass-loss. Because of this, the mass (B1) seems to be constant.

C Inlist files

In this section, the input files used for the primary input parameters and the binary input parameters are shown.

C.1 Primary Inlist file

This is the inlist file for the primary star. It contains the parameters used in the B0 & B1 models.

C.1.1 Non-magnetic (B0)

```
&star_job

      show_log_description_at_start = .true.

      pgstar_flag = .false.
```

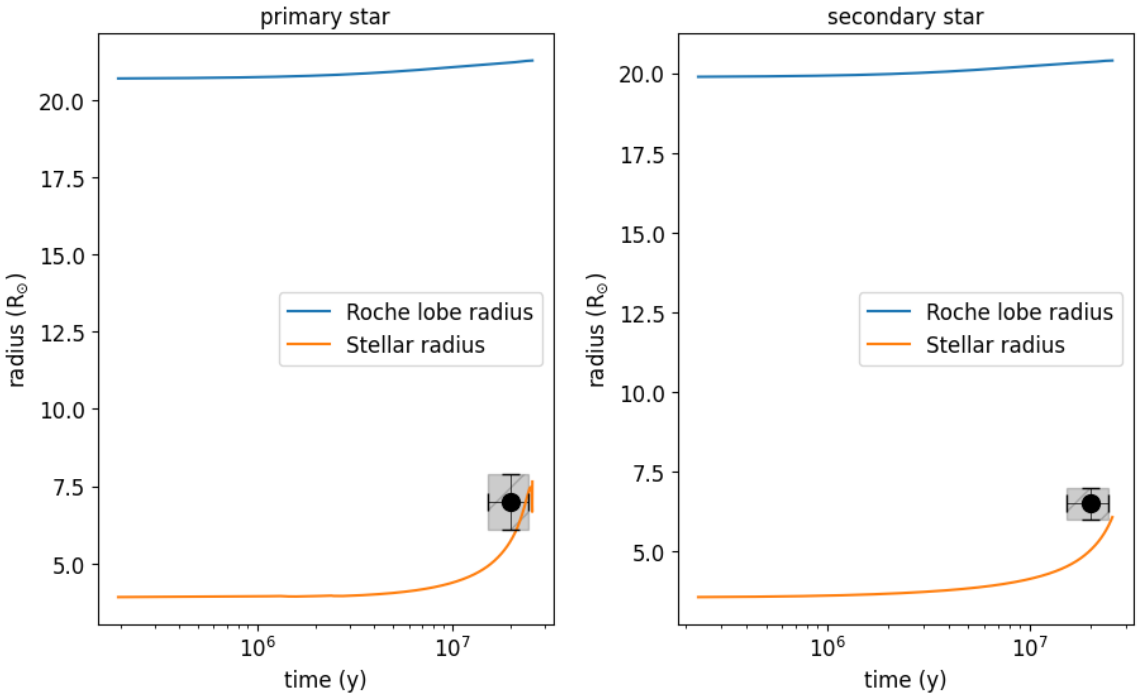

Figure 14: The radius-time plane for the primary star (left) and the secondary star (right) during the main-sequence evolution. The markers shown in the figure are the observed values and uncertainties of HD 149277. The model has been fitted to these observed values for HD 149277. For the magnetic (B1) model, the stellar and Roche lobe radii of both the primary and secondary of the HD 149277 system have been shown. The Roche lobe is always bigger than the radius of the star for both the primary and secondary.

```
      new_rotation_flag = .true.
      change_rotation_flag = .true.
      new_surface_rotation_v = 30
      set_surface_rotation_v = .true.
      set_initial_surface_rotation_v = .true.

/ ! end of star_job namelist

&controls

      extra_terminal_output_file = 'log1'
      log_directory = 'LOGS1'

      profile_interval = 1000000
      history_interval = 1
      terminal_interval = 1000000
      photo_interval = 1000000
      write_header_frequency = 1000000
```

```
hot_wind_scheme = 'Dutch'

cool_wind_full_on_T = 0.8d4
hot_wind_full_on_T = 1.2d4

Dutch_scaling_factor = 1.d0

! APPLY MASS-LOSS QUENCHING
! AND ROTATIONAL ENHANCEMENT
use_other_wind =  .false. ! OFF
mdot_omega_power = 0.0    ! This needs to be set to
                          ! enable the f_rot factor
                          ! in the run_star_extras
                          ! to work solely otherwise
                          ! two different rotational
                          ! enhancements are applied
                          ! at the same time

! APPLY MAGNETIC BRAKING
use_other_torque = .false.    ! ON
use_other_am_mixing = .false. ! ON
   ! (simplified version for AM transport enforcing
   ! solid-body rotation)

am_nu_factor = 1.d0
am_D_mix_factor = 0.033  ! mixing efficiency
                         ! (f_c in literature)
am_gradmu_factor = 0.05 ! f_mu

! factor for rot.instabilities ---> D_mix = diffusion
!     coefficient --> this is multiplied by f_c
!  D_mix = D_mix_nonrot + am_D_mix_factor *
!     ( D_SI + ...)
!     this is f_c from Heger et al

! CHEMICAL MIXING
D_DSI_factor = 1 ! dynamical shear instability
D_SH_factor = 1  ! Solberg-Hoiland
D_SSI_factor = 1 ! secular shear instability
D_ES_factor = 1  ! Eddington-Sweet circulation
D_GSF_factor = 1 ! Goldreich-Schubert-Fricke
D_ST_factor = 0  ! Spruit-Tayler dynamo

! ANGULAR MOMENTUM
```

```
      am_nu_DSI_factor = 1 ! this is for ang.mom. transport
      am_nu_SH_factor = 1
      am_nu_SSI_factor = 1
      am_nu_ES_factor = 1
      am_nu_GSF_factor = 1
      am_nu_ST_factor = 0  ! dynamo turned OFF

      xa_central_lower_limit_species(1) = 'h1'
      xa_central_lower_limit(1) = 1d-5


/ ! end of controls namelist
```

C.1.2 Magnetic (B1)

```
! inlist_test_rlo


&star_job

      show_log_description_at_start = .true.

      pgstar_flag = .false.

      new_rotation_flag = .true.
      change_rotation_flag = .true.
      new_surface_rotation_v = 300
      set_surface_rotation_v = .true.
      set_initial_surface_rotation_v = .true.

      set_initial_age = .true.
      initial_age = 0

      set_initial_model_number = .true.
      initial_model_number = 0

      extras_lrpar = 3
      extras_rpar(1) = 1.0d4 ! B0 initial polar magnetic
                             !      field strength in gauss
      extras_rpar(2) = 1.d0  ! Beff = efficiency of
                             !      magnetic braking
      extras_rpar(3) = 1.d0  ! Deceff = efficiency of
                             ! magnetic field decay
```

```
                              ! B0*exp(- Deceff * star_age/12d6)
                                   ! where t_ms = 12d6 is
                                   ! tailored for tau Sco's
                                   ! approx. ms lifetime.

      extras_lcpar = 2
      ! torque_method:
      extras_cpar(1) = 'UNIFORM_TORQUE'
            !'SURFACE_TORQUE'   ! (see run star extras)
      ! magnetic field evolution
      extras_cpar(2) = 'CON'
            ! CON or DEC for magnetic flux conservation or
            ! field decay

/ ! end of star_job namelist

&controls

      extra_terminal_output_file = 'log1'
      log_directory = 'LOGS1'

      profile_interval = 1000000
      history_interval = 1
      terminal_interval = 1000000
      photo_interval = 1000000
      write_header_frequency = 1000000

      ! APPLY MASS-LOSS QUENCHING
      ! AND ROTATIONAL ENHANCEMENT
      use_other_wind =  .true. ! OFF
      mdot_omega_power = 0.0   ! This needs to be set to
                               ! enable the f_rot factor in
                               ! the run_star_extras to
                               ! work solely otherwise two
                               ! different rotational
                               ! enhancements are applied
                               ! at the same time

      ! APPLY MAGNETIC BRAKING
      use_other_torque = .true.    ! ON
      use_other_am_mixing = .true. ! ON
            ! (simplified version for AM transport
            ! enforcing solid-body rotation)

      am_nu_factor = 1.d0
```

```
      am_D_mix_factor = 0.033  ! mixing efficiency
                               ! (f_c in literature)
      am_gradmu_factor = 0.05 ! f_mu

      ! factor for rot.instabilities ---> D_mix = diffusion
      !     coefficient --> this is multiplied by f_c
      ! D_mix = D_mix_nonrot + am_D_mix_factor *
      !     ( D_SI + ...)
      !     this is f_c from Heger et al

      ! CHEMICAL MIXING
      D_DSI_factor = 1 ! dynamical shear instability
      D_SH_factor = 1  ! Solberg-Hoiland
      D_SSI_factor = 1 ! secular shear instability
      D_ES_factor = 1  ! Eddington-Sweet circulation
      D_GSF_factor = 1 ! Goldreich-Schubert-Fricke
      D_ST_factor = 0  ! Spruit-Tayler dynamo

      ! ANGULAR MOMENTUM
      am_nu_DSI_factor = 1 ! this is for ang.mom. transport
      am_nu_SH_factor = 1
      am_nu_SSI_factor = 1
      am_nu_ES_factor = 1
      am_nu_GSF_factor = 1
      am_nu_ST_factor = 0  ! dynamo turned OFF

      xa_central_lower_limit_species(1) = 'h1'
      xa_central_lower_limit(1) = 1d-5

/ ! end of controls namelist
```

C.2 Binary Inlist file

This is the inlist file for the binary system. It contains the parameters used in the B0 & B1 models.

C.2.1 Non-magnetic (B0)

```
&binary_job

   inlist_names(1) = 'inlist1'
   inlist_names(2) = 'inlist2'

   evolve_both_stars = .true.

/ ! end of binary_job namelist
```

```
&binary_controls

   m1 = 8.81d0  ! donor mass in Msun
   m2 = 8.01d0 ! companion mass in Msun
   initial_period_in_days = 11.3708

   initial_eccentricity = .2361d0
   do_tidal_circ = .true.
   circ_type_1 = 'Hut_rad'
   circ_type_2 = 'Hut_rad'

   do_tidal_sync = .true.
   do_j_accretion = .true.
   ! be 100% sure MB is always off
   do_jdot_mb = .false.
   do_jdot_missing_wind = .true.

   sync_type_1 = 'Hut_rad'
   sync_type_2 = 'Hut_rad'

   history_interval = 1
   terminal_interval = 1000000
   photo_interval = 1000000
   write_header_frequency = 1000000

   !transfer efficiency controls
   limit_retention_by_mdot_edd = .false.

   max_tries_to_achieve = 20

/ ! end of binary_controls namelist
```

C.2.2 Magnetic (B1)

```
&binary_job

   inlist_names(1) = 'inlist1'
   inlist_names(2) = 'inlist2'

   evolve_both_stars = .true.

/ ! end of binary_job namelist

&binary_controls
```

```
   m1 = 8.7501d0  ! donor mass in Msun
   m2 = 8.012d0 ! companion mass in Msun
   initial_period_in_days = 11.08045

   initial_eccentricity = .2360

   do_tidal_circ = .true.
   circ_type_1 = 'Hut_rad'
   circ_type_2 = 'Hut_rad'

   do_tidal_sync = .true.
   do_j_accretion = .true.
   ! be 100% sure MB is always off
   do_jdot_mb = .false.
   do_jdot_missing_wind = .true.

   sync_type_1 = 'Hut_rad'
   sync_type_2 = 'Hut_rad'

   history_interval = 1
   terminal_interval = 1000000
   photo_interval = 1000000
   write_header_frequency = 1000000

   !transfer efficiency controls
   limit_retention_by_mdot_edd = .false.

   max_tries_to_achieve = 20

/ ! end of binary_controls namelist
```